

Quantum emitters in van der Waals α -MoO₃

Jeonghan Lee,^{1,2#} Haiyuan Wang,^{3#} Keun-Yeol Park,¹ Soonsang Huh,^{1,2} Donghan Kim,^{1,2}

Mihyang Yu,^{1,2} Changyoung Kim,^{1,2} Kristian Sommer Thygesen,^{3} and Jieun Lee,^{1,2*}*

¹Department of Physics and Astronomy, Seoul National University, 08826 Seoul, Korea

²Center for Correlated Electron Systems, Institute for Basic Science, 08826 Seoul, Korea

³Computational Atomic-Scale Materials Design (CAMD), Department of Physics, Technical University of Denmark, 2800 Lyngby, Denmark

These authors contributed equally to this work.

* To whom correspondence should be addressed, lee.jieun@snu.ac.kr, thygesen@fysik.dtu.dk

Single-photon emitter, van der Waals material, transition metal oxide.

Quantum emitters in solid-state materials are highly promising building blocks for quantum information processing and communication science. Recently, single-photon emission from van der Waals materials has been reported in transition metal dichalcogenides and hexagonal boron nitride, exhibiting the potential to realize photonic quantum technologies in two-dimensional materials. Here, we report the observation of single-photon generation from exfoliated and thermally annealed single crystals of van der Waals α -MoO₃. The second-order correlation function measurement displays a clear photon antibunching, while

the luminescence intensity exceeds 100 kcounts/s and remains stable under laser excitation. Also, the zero-phonon lines of these emitters are distributed in a spectrally narrow energy range. The theoretical calculation suggests that an oxygen vacancy defect is a possible candidate for the observed emitters. Together with photostability and brightness, quantum emitters in α -MoO₃ provide a new avenue to realize photon-based quantum information science in van der Waals materials.

Quantum emitters are central resources for a variety of quantum technologies [1], including quantum sensing [2], computing [3], and communication [4]. Single-photon emitters have been reported in solid-state systems like color centers in diamond [5] and silicon carbide [6], quantum dots [7], and recently in van der Waals materials [8]. For van der Waals materials, quantum emission has been reported in transition metal dichalcogenides (TMDCs) [9-11] and hexagonal boron nitride (*h*-BN) [12, 13]. Because of versatile fabrication processes and possibility of numerous heterostructure formations, 2D quantum emitters are expected to enable a wide range of novel functionalities in quantum applications. For examples, stacking two different monolayer TMDCs to form moiré structure has enabled the generation of single-photon emitters that are highly tunable [14] and spin defects found in *h*-BN [15] allow proximity-induced sensitive quantum sensing and microscopy of nearby specimens [16, 17]. However, so far quantum emitters in van der Waals materials have been reported in only a few material platforms [18], which motivates the search for single-photon emitters in a wider material range and the identification of their electronic structures.

α -MoO₃ is a van der Waals material and the only layered crystal among its polymorphs. Figure 1a illustrates the structure of α -MoO₃ consisting of bilayers of covalently bonded MoO₆

octahedra. The MoO₆ octahedra bilayers are held together by weak van der Waals forces, forming an orthorhombic crystal structure. α -MoO₃ exhibits unique physical properties such as a wide bandgap (~ 3 eV) [19], high electron mobilities [20], and mechanical flexibility [21], which have led to advancements in various applications including photodetectors [22], field-effect transistors [23], and wearable electronics [24]. Furthermore, anisotropic optical response of α -MoO₃ has enabled tunable light-matter interactions in this material through multilayer stacking [25]. These electrical and optical characteristics of α -MoO₃ are expected to be promising for nanostructured quantum device implementations in van der Waals platforms. However, studies on quantum defects and the possibility of quantum light generation in α -MoO₃ have not yet been reported.

In this work, we show the generation of single photons from atomic defects in layered α -MoO₃ and study their electronic and optical properties. The observed emitters in α -MoO₃ show high emission intensity and photostability, with the luminescence intensity observable up to room temperature. The zero-phonon line of these emitters is found to be predominantly distributed in a narrow energy range around 2.2 eV. By calculating the photoluminescence spectrum, we identify an oxygen vacancy as a highly probable origin of the observed quantum emitters. Our work thus demonstrates α -MoO₃ as a new platform to study quantum defects and single-photon emitters in layered structures for van der Waals material based quantum technologies.

The bulk α -MoO₃ crystal is grown by the Bridgman technique (details in method) and characterized by high-resolution X-ray diffraction (XRD) and Raman spectroscopy. Figure 1b shows the XRD measurement of an as-grown crystal. Three peaks were observed at 12.68°, 25.64°, and 38.94°, which correspond to the indices of (020), (040), and (060), respectively [26]. Other peaks were not observed which supports the high crystallinity of the synthesized crystal. We additionally checked the Raman spectrum to validate the crystal structure. The measured spectrum

shown by a blue solid line in Figure 1c is identical to the Raman measurement data of an orthorhombic α -MoO₃ [27], providing additional confirmation of the absence of other phases.

We obtained thin layers of α -MoO₃ flakes by the mechanical exfoliation of bulk crystals onto silicon substrates. Figure 1d shows the optical microscope image of an exfoliated α -MoO₃ flake, in which sharp edges can be easily identified following the crystal structure. The thickness of exfoliated α -MoO₃ thin flakes was measured with atomic force microscopy (AFM) as shown in the inset. The obtained flakes were then annealed at 300 °C to produce optically active defect sites as described in the method section. After annealing, the Raman spectrum was measured, showing a negligible change in the peak frequencies (red solid line in Figure 1c). This indicates that the crystal structure is retained after the heating process. Some samples were subsequently spin-coated with a polymer to protect their surfaces. By a polymer coating, any potential damage to the flakes is prevented and overall photostability of α -MoO₃ emitters could be improved.

For optical measurements, we used a scanning confocal microscopy set-up which is shown in the inset of Figure 2a. The samples were kept in a cryostat at a temperature of 10 K for all measurements unless otherwise noted. By scanning with a sub-bandgap continuous-wave laser centered at 532 nm (2.33 eV), spatially localized emission is measured from several different spots of α -MoO₃ flakes. Figure 2a shows the spectrum of one of the emitters which has a zero-phonon line (ZPL) at 563 nm (2.20 eV) with multiple phonon side bands at longer wavelengths. Emission spectra measured from several other emitters are displayed in supplementary section 1 which have emission wavelength similar to this emitter.

Interestingly, most emitters that we observed are found to have ZPL energy predominantly around 2.2 eV (Figure 2b). From the Gaussian fitting of the distribution of the emission energy,

the central ZPL energy was 2.18 eV with standard deviation of 230 meV. Unlike *h*-BN which has a wide range of emission spectra among different emitters [28], the emitters found in α -MoO₃ have a narrow distribution of photon energy similar to quantum emitters in diamond NV centers [5] and silicon carbide [6]. This suggests the possibility of homogeneous origin for emitters found in this material.

By calculating the Debye-Waller factor for about two dozen of emitters, we found that the average ratio of the ZPL emission to total emission was about 0.2, showing that a large portion of the emission is channeled into the ZPL. From these emitters, we estimated the average Huang-Rhys (HR) factor to be about 1.9, which is comparable to electron-phonon coupling strength found in other solid-state quantum emitters (detail distributions in supplementary section 2).

Next, we confirm the single-photon characteristics of the observed emitters by the second-order correlation function $g^2(\tau)$ detection using the Hanbury-Brown-Twiss (HBT) interferometer. In Figure 2c, the measured $g^2(\tau)$ curve for the emitter shown in Figure 2a reveals a dip well below 0.5 at $\tau = 0$. To extract information from the $g^2(\tau)$ curve, we fitted the obtained data using a three-level model formula [12],

$$g^2(\tau) = 1 - p[(1 + a)e^{-|\tau|/\tau_1} - ae^{-|\tau|/\tau_2}]. \quad (1)$$

Here, a and p are fitting parameters while τ_1 and τ_2 are the lifetime of the excited and meta-stable states, respectively. The $g^2(0)$ of this emitter was 0.15 ± 0.05 , demonstrating the quantum nature of the emitted light. This value is obtained after correcting for the background following the procedure described in supplementary section 3 [29]. The extracted excited state and meta-stable state lifetime of the emitter were 3.74 ns and 8.28 μ s, respectively. The antibunching characteristics were also verified for several other emitters, as demonstrated in supplementary

section 1. We also measured $g^2(\tau)$ at various excitation powers for one emitter to investigate the photophysics and dynamics of the emission process, which is described in supplementary section 4. Most of the quantum emitters in our experiment are found in thin α -MoO₃ flakes with thickness ranging between 3.5 and 30 nm. For the lower bound, we observed a quantum emitter from a 5-layer sample which was the thinnest flake that we could obtain from exfoliation (supplementary section 5).

By performing the power dependence measurement of the emitter shown in Figure 2a, we determined the saturating behavior of the luminescence. In Figure 2d, the emission rate is depicted as a function of the laser excitation power. The experimental data was fitted using the following equation,

$$I(P) = I_{\text{sat}} \frac{P}{P + P_{\text{sat}}} \quad (2)$$

where I is the emission count rate and P is the incident laser power. I_{sat} and P_{sat} are the maximal emission count rate and the saturation power, respectively. The fitting result shows that P_{sat} and I_{sat} are 199 μW and 410 kcounts/s, respectively. Considering the collection efficiency (~ 0.027) of our set-up along the path to the spectrometer, the actual I_{sat} is calculated to be about 15 Mcounts/s, demonstrating the high emission intensity. A comparable emission rate has been observed previously for quantum emitters in silicon nitride and gallium nitride [30, 31]. We expect that further improvements can be made through integration with optical cavities or plasmonic nanostructures for more efficient light extraction [32].

We then carried out several measurements to characterize the optical properties of α -MoO₃ quantum emitters. As displayed in Figure 3a, we obtained the lifetime of an emitter using a time-

resolved measurement with a pulse laser excitation centered at 532 nm. The lifetime of the emitter was found to be about 3 ns, quantitatively agreeing with τ_1 obtained from Figure 2c and supplementary section 1.

In Figure 3b, the emission stability test result is displayed, which shows the stable emission with minimal photon blinking or bleaching. The simultaneous collection of the photon energy and evolution time reveals that the ZPL energy and intensity of the emitter remain mostly unchanged. The wavelength range indicated by the dashed line in Figure 3b was filtered and measured by using a single-photon counting module (SPCM). The corresponding time trace result is shown in Figure 3c, demonstrating the absence of the intensity degradation over time. We note that data from all emitters that we show in the main text originate from samples that are polymer-coated, which exhibited outstanding photostability compared to the emitters in bare samples. We show the spectrum and photostability test result of emitters from bare α -MoO₃ flakes for comparison in supplementary section 6. The enhanced photostability could have been induced by the polymer coating that alters the bonding interface near the emitter site [33].

The emission polarization dependence measurement is also performed to get structural information of the emitter. Figure 3d and 3e exhibit the emission spectra measured while varying the excitation and emission photon polarization angles, respectively. Almost identical polarization dependence is found for both ZPL and phonon side bands, confirming that these peaks originate from the same emitter. Also, both excitation and emission polarization directions are closely aligned as can be seen in the polar plot (Figure 3f). Furthermore, the two-fold symmetry of the polarization dependence shows that the photons are linearly polarized, which suggests the existence of structural anisotropy in the crystal structure of the quantum emitter.

To gain insight into the origin of the observed quantum emitters, we now turn to the theoretical investigation of the defect structure. As the hydrogen gas used during the annealing process can cause the reduction of α -MoO₃ [34], it is highly probable that oxygen vacancy defects are responsible for the observed emitters. In the crystal structure of α -MoO₃, there are three inequivalent oxygen sites: O₁, O₂, and O₃ that are singly, doubly, and triply coordinated by the Mo atoms, respectively (see Figure 1a). Therefore, three types of oxygen vacancies can be formed, which are referred to as V₁, V₂, and V₃. To simulate the defect models, we performed density functional theory (DFT) calculations using the Vienna *ab initio* simulation package (VASP) [35]. In the simulation, we employed the Perdew-Burke-Ernzerhof (PBE) functional [36] to optimize the crystal geometry while the Heyd-Scuseria-Ernzerhof (HSE06) hybrid functional [37] was used to obtain the electronic properties (denoted as HSE06@PBE to stress that the structure is optimized with the PBE functional). More details can be found in methods and supplementary section 7. Using the HSE06@PBE, we determined the band gap of the bulk α -MoO₃ to be 3.0 eV in excellent agreement with the experimental value of 3.2 eV [19].

We calculated the formation energy of the three different vacancy sites in various charge states ($q = +2, +1, 0, -1, -2$) and found that V₃ is significantly less stable than the other two vacancy sites (details in supplementary section 7.1). Notably, V₁ and V₂ have very similar formation energies deviating by less than 0.2 eV (refer to Figure S7 in supplementary section 7.1). The formation energy of V₂, as a representative, is shown in Figure 4a. In general, both V₁ and V₂ undergo charge state transitions shifting from +2 to +1 and finally to the neutral state as the Fermi level moves upwards from the valence band maximum. The vacancy sites are found to be most stable in their +2 and +1 charge states with compensating electrons in the conduction band. This agrees well with the observed *n*-type characteristics of α -MoO₃ [38]. Based on their higher stability,

we focus on V_1 and V_2 in their positive and neutral charge states for the following electronic property investigations.

From our DFT calculations, we have identified the defect V_2 in the charge state $q = +2$, namely V_2^{+2} , to be the most probable origin of the observed quantum emitter (Figure 4b). Details can be found in the supplementary section 7.2. The calculated single-particle energy level of the V_2^{+2} defect is shown in Figure 4c. It demonstrates that the ground state is a singlet and that the energy difference between the highest occupied orbital and lowest unoccupied orbital is 1.91 eV in good agreement with the measured photon emission energies. From the calculated inverse participation ratio (IPR), which is a commonly used measure for the degree of orbital localization [39], we found that the lowest unoccupied orbital (excited state of the emitter) is well localized while the highest occupied orbital is delocalized, or partially localized corresponding to a shallow defect state (see supplementary Figure S12). We further performed a self-consistent field calculation (Δ SCF) with an electron promoted from the highest occupied to the lowest unoccupied orbital to obtain the ZPL energy and the HR factor of V_2^{+2} . The calculated ZPL energy is 1.8 eV which is slightly smaller but in reasonable agreement with experiments. The calculated HR factor of 3.59 is fully consistent with the high luminosity of the optically active quantum emitters and agrees well with the value estimated from the experimental data (supplementary section 2). For V_2 in other charge states and for the other oxygen vacancies, the calculated ZPL energies and HR factors were in less good agreement with the experimental observations.

Focusing on the V_2^{+2} defect, we show the calculated emission spectrum [40] in Figure 4d (the calculated spectrum has been shifted to match the ZPL of the experiment). The similarity between the theoretical and experimental line shapes is striking. The most pronounced phonon side bands are observed within approximately 200 meV of the ZPL. The calculated electron-

phonon spectral density is shown in supplementary section 7.3. An analysis of the localized defect state (the lowest unoccupied orbital on Fig. 4c) shows that it is mainly composed of d-orbitals of the Mo atoms close to the O vacancy, consistent with a previous report [41]. We further calculated the transition dipole moment between the highest occupied state and lowest unoccupied state. The calculated dipole moment showed a linear polarization of the form $\mathbf{p} = \mathbf{a} + \mathbf{c}$ (with the crystal axes defined in Fig. 1a). It is difficult to compare this polarization directly to the experiments because the measured polarization differs from emitter to emitter due to variations in the local crystal symmetry of the defects, which are often located at the edges of the flakes.

Lastly, we discuss the temperature dependence of the observed α -MoO₃ quantum emitters. From the temperature dependence measurement, the luminescence intensity of the emitters was observable not only at cryogenic temperatures but also at elevated temperatures. Details are in supplementary section 8. As the temperature increases, the spectrum shows the characteristic energy shift and linewidth broadening of the ZPL also observed for other solid-state quantum emitters [42]. The emission intensity decreases with increasing temperature, but a finite luminescence was observable at room temperature. We note that the $g^2(\tau)$ curve was observable up to 77 K, suggesting a high possibility to achieve α -MoO₃ quantum emission at room temperature by improving the sample preparation process and engineering the emitter's dielectric environment.

In conclusion, we have identified and characterized single-photon emitters with high intensity and photostability in thin layers of α -MoO₃. Our DFT calculations indicate that the origin of the quantum emitters is likely to be oxygen vacancy defects. We found that the surface treatment can further stabilize the emission properties. Moreover, the emission from defect centers were observable up to room temperature. Because of a large band gap and accessibility to electrical

modulation, α -MoO₃ can be utilized for development of quantum devices with novel optoelectronic functionalities. Through van der Waals stacking with other layered materials, α -MoO₃ opens new opportunities for 2D material based quantum nanophotonics and information science.

Methods

Crystal Growth

Single crystals of α -MoO₃ were synthesized using the modified Bridgman method [43]. α -MoO₃ powder (99.9995%) was loaded into quartz tube and then sealed in the air. The sealed tube was heated to 855 °C at a rate of 120 °C/hour and held at the same temperature for 3 hours. The growth was initiated at a rate of 1.6 mm/hour in the temperature gradient of 3 to 5 °C/cm. After complete solidification, the furnace was cooled to room temperature at a rate of 15 °C/hour.

Sample Fabrication

Thin layer α -MoO₃ flakes were mechanically exfoliated from bulk onto SiO₂ on Si substrates. Exfoliated flakes were annealed in a tube furnace at 300 °C in the pressure of 10 Torr under flowing Ar gas for 30 mins. The flow rate was 500 sccm. The samples were cooled down to room temperature under the vacuum. For the polymer-coating, samples were spin-coated using polymethyl methacrylate (PMMA) at 5000 rpm for 60 s.

Optical Measurements

For photoluminescence (PL) measurements, we used a home-built confocal microscopy [44]. The emitters are excited with a continuous-wave 532 nm solid-state laser with power less than 20 μ W except power dependent measurements. The laser is incident onto the sample through an objective

lens (x60, NA = 0.7) and the emitted light is collected through the same objective lens and directed to a spectrometer. Samples were loaded in a cryostat with temperature varying from 6 to 298 K. An XY-piezo stage inside the cryostat was employed to move the sample position to perform 2D spatial scanning and locate emitters. The polarization dependence measurement was carried out by selecting the polarization of light using a Glan-Taylor polarizer and rotating the polarization angle by a half-wave plate (HWP).

For the second-order correlation measurement, a flip mirror in the collection path before the spectrometer guided the emission to the HBT interferometer. The emitted light from α -MoO₃ flakes was filtered using multiple bandpass filters, split by a beam splitter and collected by two single-photon counting modules (SPCMs). The signals were processed by a time-correlated single-photon counting (TCSPC) instrument for correlation measurement with the time resolution of 350 ps.

For the time-resolved PL measurement, a femtosecond laser with a pulse width of 140 fs and repetition rate of 80 MHz was used. The laser pulse of 1064 nm wavelength was frequency-doubled using a beta barium borate (BBO) crystal to produce 532 nm pulse. During the measurement, the pulse laser power was kept at 2.5 μ W. SPCMs and a TCSPC were used to obtain the histogram of collected photons.

For Raman spectroscopy, we used a room temperature confocal microscopy set-up with an objective lens (40x, NA = 0.6). A 532 nm continuous-wave laser with the power of 50 μ W was used as an excitation source. In the collection path, a longpass filter was employed to remove the laser line and a spectrometer is used for recording Raman spectra.

DFT Calculation

All the calculations were performed with Vienna *ab initio* simulation package (VASP) [35], which employs density functional theory (DFT) [45] with projector augmented wave (PAW) method [46]. Constrained DFT methodology is used for the excited state calculations [47]. All the calculations are spin-polarized, and the geometries are fully relaxed with van der Waals correction (vdw-D3) [48]. The semi-local exchange-correlation functional of Perdew-Burke-Ernzerhof (PBE) [36] and the screened hybrid functional of Heyd-Scuseria-Ernzerhof (HSE06) with the standard mixing parameter $\alpha = 0.25$ are employed to optimize the geometries [37]. The total energy convergence criterion is set at 10^{-7} eV for PBE and 10^{-6} eV for HSE06, while the structure minimization criterion is set at 10^{-4} for PBE and 0.03 eV/Å for HSE06. In the case of HSE06@PBE for the results shown in the main text, the electronic properties are established through self-consistent one-shot calculations employing the HSE06 functional with geometries optimized using PBE. For benchmark, we also performed the ionic and electronic relaxation using the full HSE06, which yields results consistent with those obtained with HSE06@PBE confirming the reliability of the atomic geometry produced by the PBE functional (supplementary section 7). The plane-wave cutoff energy of 400 eV and a $1 \times 2 \times 2$ k-point grid for the $1 \times 3 \times 3$ supercell (144 atoms) are adopted. For the V_2^{+2} vacancy, we perform the entire computational analysis using the PBE xc-functional and a larger ($1 \times 4 \times 4$) supercell to reduce the influence of finite size effects. The phonons of the supercell are calculated using the finite displacement method, as implemented in the PHONOPY software package [49] under the PBE functional. We assume that the phonons remain the same in the ground and excited states, which forms the basis of the method used to calculate the PL spectrum.

Acknowledgements

This work was supported by the National Research Foundation (NRF) of Korea (Grants No. 2020R1A2C201133414 and No. 2021R1A5A103299613). Measurements were supported by the Institute for Basic Science (IBS) of Korea (Grant No. IBS-R009-D1-2023-a00) and the Ministry of Science and ICT (MSIT) of Korea under the Information Technology Research Center (ITRC) support program (Grant No. RS-2022-00164799). J. L. acknowledges the support from the Creative-Pioneering Researchers Program through Seoul National University. H. W. and K. S. T. acknowledge the support of Novo Nordisk Foundation Challenge Programme 2021: Smart nanomaterials for applications in life-science, BIOMAG Grant NNF 21OC0066526. K. S. T. is a Villum Investigator supported by VILLUM FONDEN (Grant No. 37789).

References

1. O'Brien, J. L., Furusawa, A. & Vučković, J. Photonic quantum technologies, *Nat. Photonics* **3**, 687-695 (2009).
2. Degen, C. L., Reinhard, F. & Cappellaro, P. Quantum sensing, *Rev. Mod. Phys.* **89**, 035002 (2017).
3. Knill, E., Laflamme, R. & Milburn, G. J. A scheme for efficient quantum computation with linear optics, *Nature* **409**, 46-52 (2001).
4. Gisin, N. & Thew, R. Quantum communication, *Nat. Photonics* **1**, 165-171 (2007).
5. Kurtsiefer, C. *et al.* Stable solid-state source of single photons, *Phys. Rev. Lett.* **85**, 290-293 (2000).
6. Castelletto, S. *et al.* A silicon carbide room-temperature single-photon source, *Nat. Mater.* **13**, 151-156 (2014).
7. Michler, P. *et al.* A quantum dot single-photon turnstile device, *Science* **290**, 2282-2285 (2000).
8. Toth, M. & Aharonovich, I. Single photon sources in atomically thin materials, *Annu. Rev. Phys. Chem.* **70**, 123-142 (2019).
9. He, Y. M. *et al.* Single quantum emitters in monolayer semiconductors, *Nat. Nanotechnol.* **10**, 497-502 (2015).
10. Koperski, M. *et al.* Single photon emitters in exfoliated WSe₂ structures, *Nat. Nanotechnol.* **10**, 503-506 (2015).
11. Chakraborty, C. *et al.* Voltage-controlled quantum light from an atomically thin semiconductor, *Nat. Nanotechnol.* **10**, 507-511 (2015).
12. Tran, T. T. *et al.* Quantum emission from hexagonal boron nitride monolayers, *Nat. Nanotechnol.* **11**, 37-41 (2016).
13. Bourrellier, R. *et al.* Bright UV single photon emission at point defects in h-BN, *Nano Lett* **16**, 4317-4321 (2016).

14. Baek, H. *et al.* Highly energy-tunable quantum light from moiré-trapped excitons, *Sci. Adv.* **6**, eaba8526 (2020).
15. Abdi, M. *et al.* Color centers in hexagonal boron nitride monolayers: a group theory and ab initio analysis, *ACS Photonics* **5**, 1967-1976 (2018).
16. Gottscholl, A. *et al.* Spin defects in hBN as promising temperature, pressure and magnetic field quantum sensors, *Nat. Commun.* **12**, 4480 (2021).
17. Healey, A. J. *et al.* Quantum microscopy with van der Waals heterostructures, *Nat. Phys.* **19**, 87-91 (2022).
18. Montblanch, A. R. *et al.* Layered materials as a platform for quantum technologies, *Nat. Nanotechnol.* **18**, 555-571 (2023).
19. Sian, T. S. & Reddy, G. B. Optical, structural and photoelectron spectroscopic studies on amorphous and crystalline molybdenum oxide thin films, *Solar Energy Materials and Solar Cells* **82**, 375-386 (2004).
20. Zhang, W. B., Qu, Q. & Lai, K. High-mobility transport anisotropy in few-layer MoO₃ and its origin, *ACS Appl. Mater. Interfaces* **9**, 1702-1709 (2017).
21. Bessonov, A. A. *et al.* Layered memristive and memcapacitive switches for printable electronics, *Nat. Mater.* **14**, 199-204 (2015).
22. Zheng, Q. *et al.* A flexible ultraviolet photodetector based on single crystalline MoO₃ nanosheets, *J. Mater. Chem. C* **3**, 7469-7475 (2015).
23. Alsaif, M. M. Y. A. *et al.* High-performance field effect transistors using electronic inks of 2D molybdenum oxide nanoflakes, *Adv. Funct. Mater.* **26**, 91-100 (2016).
24. Choi, D. K. *et al.* Highly efficient, heat dissipating, stretchable organic light-emitting diodes based on a MoO₃/Au/MoO₃ electrode with encapsulation, *Nat. Commun.* **12**, 2864 (2021).
25. Hu, G. *et al.* Topological polaritons and photonic magic angles in twisted α -MoO₃ bilayers, *Nature* **582**, 209-213 (2020).
26. Kim, J. H. *et al.* van der Waals epitaxial growth of single crystal α -MoO₃ layers on layered materials growth templates, *2D Mater.* **6**, 015016 (2018).
27. Wen, M. *et al.* In-plane anisotropic Raman spectroscopy of van der Waals α -MoO₃, *J. Phys. Chem. C* **125**, 765-773 (2020).
28. Tran, T. T. *et al.* Robust multicolor single photon emission from point defects in hexagonal boron nitride, *ACS Nano* **10**, 7331-7338 (2016).
29. Fuchs, F. *et al.* Engineering near-infrared single-photon emitters with optically active spins in ultrapure silicon carbide, *Nat. Commun.* **6**, 7578 (2015).
30. Senichev, A. *et al.* Room-temperature single-photon emitters in silicon nitride, *Sci. Adv.* **7**, eabj0627 (2021).
31. Berhane, A. M. *et al.* Bright room-temperature single-photon emission from defects in gallium nitride, *Adv. Mater.* **29** (2017).
32. Tomm, N. *et al.* A bright and fast source of coherent single photons, *Nat. Nanotechnol.* **16**, 399-403 (2021).
33. Bradac, C. *et al.* Observation and control of blinking nitrogen-vacancy centres in discrete nanodiamonds, *Nat Nanotechnol* **5**, 345-349 (2010).
34. Kong, H. *et al.* Reductive-annealing-induced changes in Mo valence states on the surfaces of MoO₃ single crystals and their high temperature transport, *Curr. Appl. Phys.* **19**, 1379-1382 (2019).

35. Kresse, G. & Furthmüller, J. Efficient iterative schemes for ab initio total-energy calculations using a plane-wave basis set, *Phys. Rev. B* **54**, 11169-11186 (1996).
36. Perdew, J. P., Ernzerhof, M. & Burke, K. Rationale for mixing exact exchange with density functional approximations, *J. Chem. Phys.* **105**, 9982-9985 (1996).
37. Krukau, A. V. *et al.* Influence of the exchange screening parameter on the performance of screened hybrid functionals, *J. Chem. Phys.* **125**, 224106 (2006).
38. Peelaers, H., Chabinye, M. L. & Van de Walle, C. G. Controlling n-type doping in MoO₃, *Chem. Mater.* **29**, 2563-2567 (2017).
39. Konstantinou, K. *et al.* Revealing the intrinsic nature of the mid-gap defects in amorphous Ge₂Sb₂Te₅, *Nat. Commun.* **10**, 3065 (2019).
40. Alkauskas, A. *et al.* First-principles theory of the luminescence lineshape for the triplet transition in diamond NV centres, *New J. Phys.* **16**, 073026 (2014).
41. Guo, Y. & Robertson, J. Origin of the high work function and high conductivity of MoO₃, *Appl. Phys. Lett.* **105** (2014).
42. Jungwirth, N. R. *et al.* Temperature dependence of wavelength selectable zero-phonon emission from single defects in hexagonal boron nitride, *Nano Lett.* **16**, 6052-6057 (2016).
43. Kong, H. *et al.* Growth and physical properties of large MoO₃ single crystals, *J. Mater. Sci.* **51**, 8928-8934 (2016).
44. Noh, G. *et al.* Stark tuning of single-photon emitters in hexagonal boron nitride, *Nano Lett.* **18**, 4710-4715 (2018).
45. Kohn, W. & Sham, L. J. Self-consistent equations including exchange and correlation effects, *Phys. Rev.* **140**, A1133-A1138 (1965).
46. Kresse, G. & Joubert, D. From ultrasoft pseudopotentials to the projector augmented-wave method, *Phys. Rev. B* **59**, 1758-1775 (1999).
47. Kaduk, B., Kowalczyk, T. & Van Voorhis, T. Constrained density functional theory, *Chem. Rev.* **112**, 321-370 (2012).
48. Grimme, S. *et al.* A consistent and accurate ab initio parametrization of density functional dispersion correction (DFT-D) for the 94 elements H-Pu, *J. Chem. Phys.* **132**, 154104 (2010).
49. Togo, A. & Tanaka, I. First principles phonon calculations in materials science, *Scr. Mater.* **108**, 1-5 (2015).

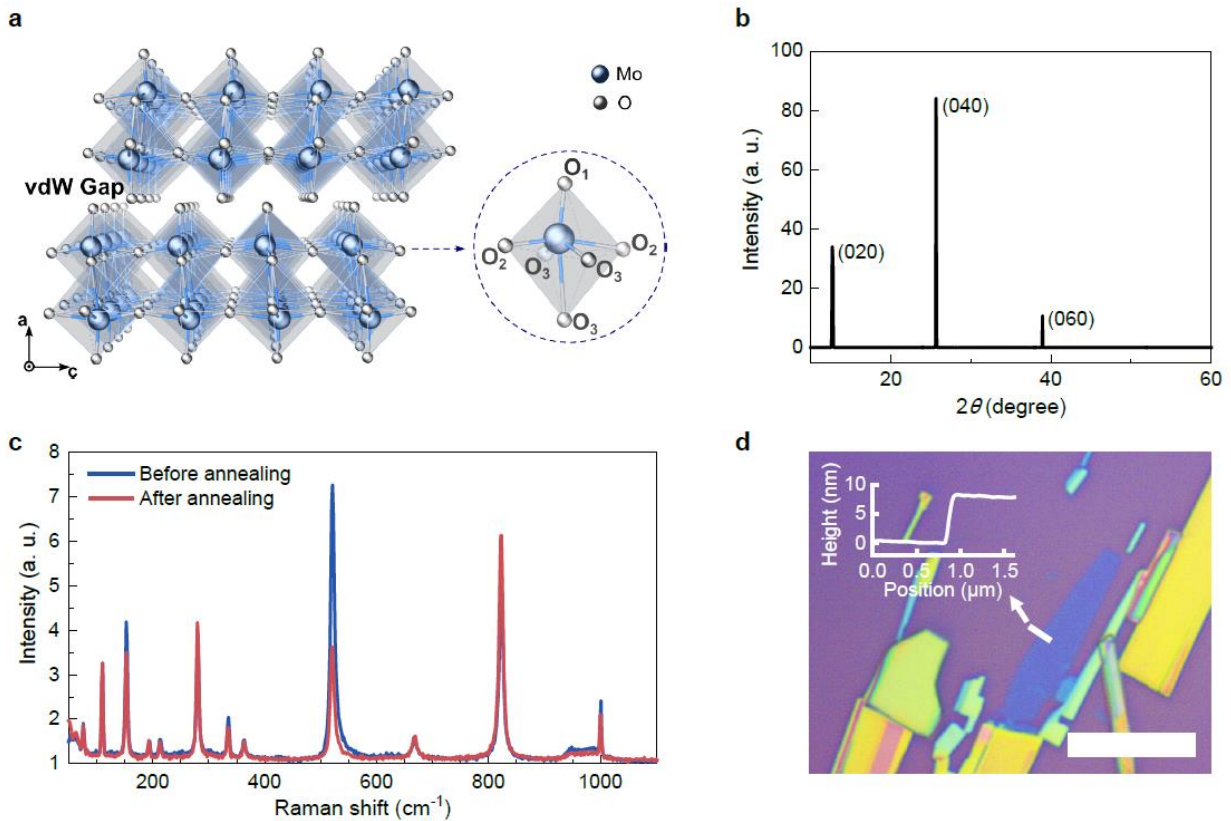


Figure 1. α - MoO_3 crystal structure and bulk characterization. (a) Illustration of α - MoO_3 lattice structure. Blue and grey balls are molybdenum and oxygen atoms, respectively. The octahedron in the right bottom panel shows the positions of three inequivalent oxygen atoms. (b) High resolution XRD measurement result of as-grown α - MoO_3 . (c) Raman spectrum of α - MoO_3 bulk flake measured before (blue solid line) and after (red solid line) thermal annealing. The peak at 520 cm^{-1} is silicon Raman peak. (d) Optical image of an exfoliated α - MoO_3 thin flake with a scale bar of $10 \mu\text{m}$. The graph in the inset shows an AFM line profile of the flake.

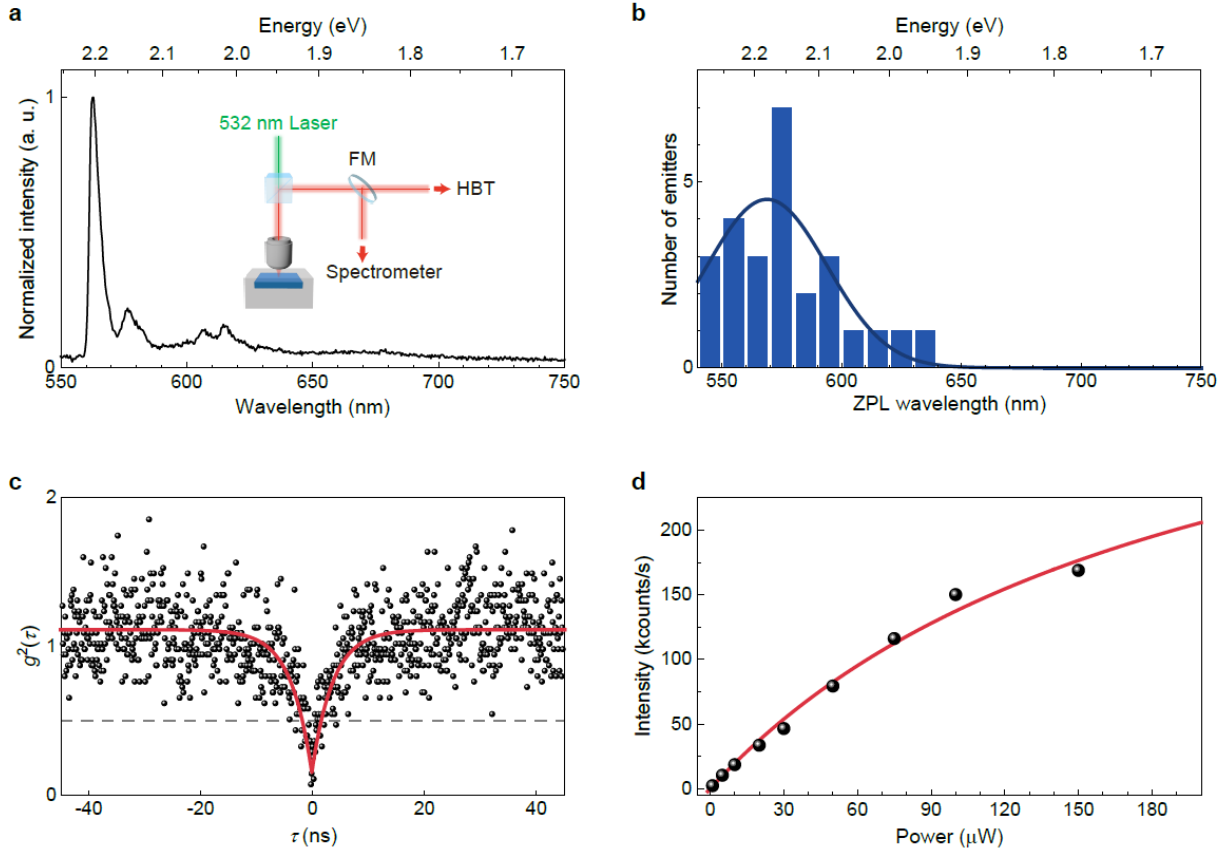


Figure 2. Single-photon emitters in α -MoO₃. (a) Photoluminescence spectrum of an emitter in α -MoO₃ measured at 10 K. The spectrum was acquired using a laser excitation power of 10 μ W. Inset shows the schematics of a home-built confocal set-up used in the experiment. A flip mirror (FM) is used to guide the emission to either spectrometer or HBT interferometer. (b) ZPL energy distribution of emitters. A Gaussian fit is shown as a solid line. (c) Second-order correlation function of the emitter shown in (a). A red solid line represents the fitting result. A dashed horizontal line at 0.5 is shown to provide the guide to the criterion for single-photon emission. During the measurement, the laser power was maintained at 10 μ W. (d) Emission intensity as a function of laser power with the fitting result depicted as a red solid line.

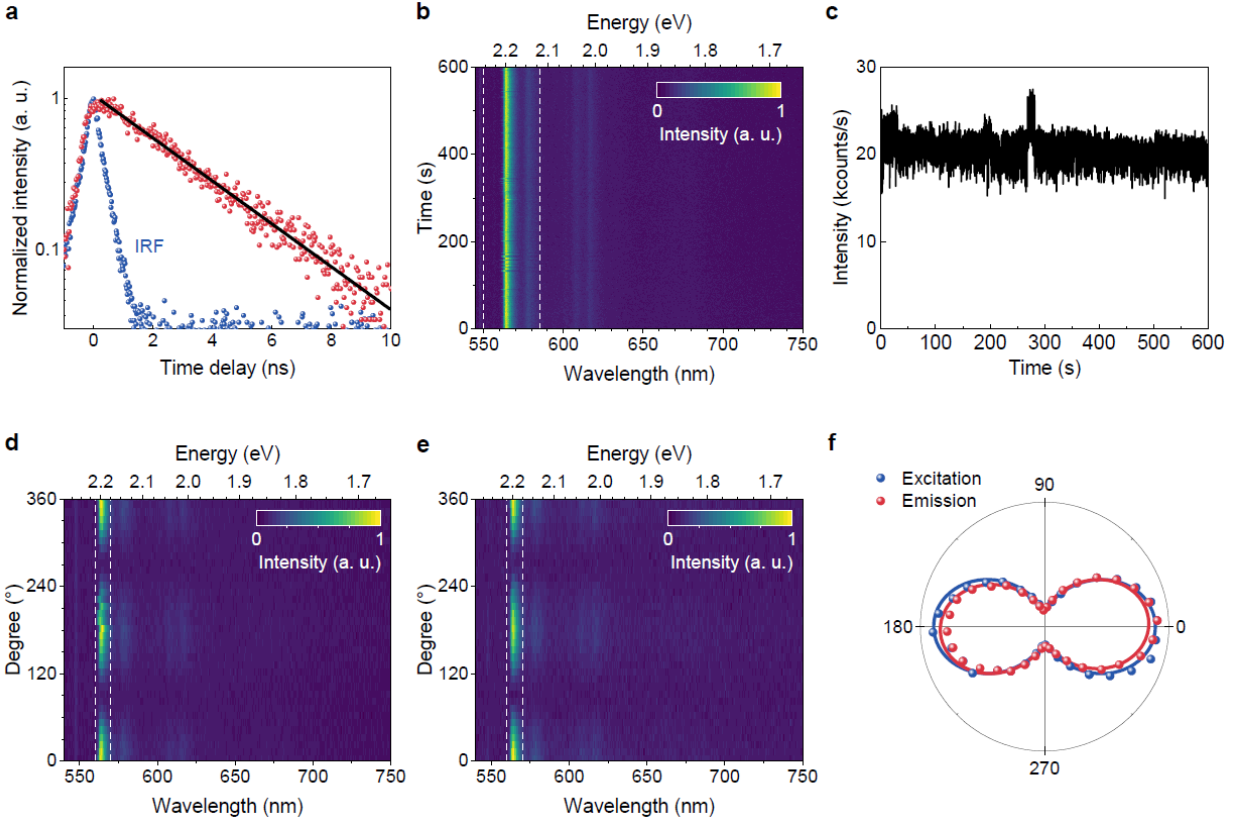


Figure 3. Optical properties of single-photon emitters. (a) Time-resolved lifetime measurement result of an emitter (red dot) measured at 10 K. The power of the pulse laser was $2.5 \mu\text{W}$. The exponential fit result (black solid line) provides an excited state lifetime of 3.07 ns. Blue dot represents the instrument response function (IRF). (b) Stability measurement of the emission intensity as a function of both time and wavelength over a duration of 10 mins. (c) Fluorescence count rates measured with SPCM in the wavelength range between the white dashed lines in (b). (d, e) Polarization dependence measurement of ZPL and phonon side band as a function of excitation laser polarization (d) and emission polarization (e), respectively. (f) Polar mapping of ZPL intensity (integrated between white dashed lines in (d) and (e)) for excitation laser polarization (blue dot) and emission polarization (red dot) dependence. Solid lines are $I(\theta) = A\sin^2(\theta - \theta_0) + B$ fit result to each data.

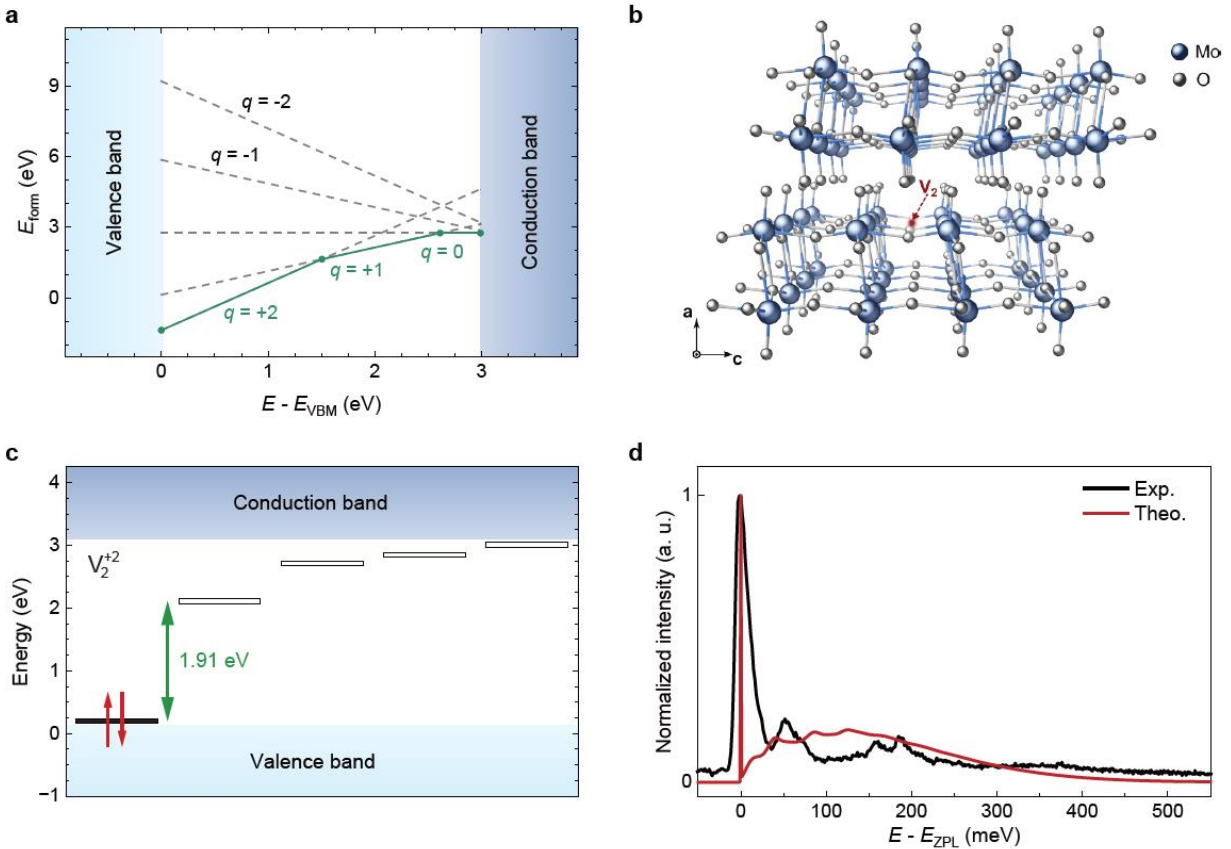


Figure 4. DFT calculation of oxygen vacancy defect center. (a) Formation energy of V_2 defect as a function of the Fermi energy (E_F). Each dashed line represents charge states encompassing +2 to -2 . The green solid line highlights the most stable charge state along the E_F . The blue region is for the valence band and the grey region is for the conduction band of the pristine α - MoO_3 . **(b)** The crystal structure of V_2^{+2} defect. **(c)** Kohn-Sham energy levels of V_2^{+2} defect. The filled and empty blocks stand for the occupied and unoccupied states, respectively, with red arrows indicating electron spins. The energy difference between the highest occupied and lowest unoccupied state is 1.91 eV. **(d)** Theoretical calculation of V_2^{+2} emission spectrum (red solid line). Spectrum of the experimentally observed emitter in Figure 2a is also shown (black solid line). The energy of both spectra is shifted horizontally from the ZPL energy to compare the shape and distribution of the phonon side band.